

# Monte Carlo Simulator to Study High Mass X-ray Binary System

S. Watanabe, F. Nagase, T. Takahashi  
*ISAS/JAXA, Sagami-hara, Kanagawa 229-8510, Japan*  
M. Sako, S.M. Kahn  
*KIPAC/Stanford, Stanford, CA 94305, USA*  
M. Ishida, Y. Ishisaki  
*Tokyo Metropolitan Univ., Hachioji, Tokyo 192-0397, Japan*  
T. Kohmura  
*Kougakuin Univ., Hachioji, Tokyo 192-001, Japan*  
F. Paerels  
*Columbia Univ., New York, NY 10027, USA*

We have developed a Monte Carlo simulator for astrophysical objects, which incorporate the transportation of X-ray photons in photoionized plasma. We applied the code to X-ray spectra of high mass X-ray binaries, Vela X-1 and GX 301-2, obtained with Chandra HETGS. By utilizing the simulator, we have successfully reproduced many emission lines observed from Vela X-1. The ionization structure and the matter distribution in the Vela X-1 system are deduced. For GX 301-2, we have derived the physical parameters of material surrounding the neutron star from fully resolved shape of the Compton shoulder in the iron  $K\alpha$  line.

## 1. Introduction

The grating spectrometers on-board *Chandra* and *XMM-Newton* have provided the high-resolution X-ray spectra of astrophysical sources. They have resolved forests of X-ray emission lines, Doppler shifted emission/absorption lines and distinguishing line profiles like Compton shoulders. The analysis of these features provides unambiguous information on physical conditions in astrophysical sources.

The high mass X-ray binaries' (HMXBs') spectra obtained with *Chandra* High Energy Transmission Grating Spectrometer (HETGS) are shown in Figure 1 and Figure 2. Figure 1 shows a spectrum of Vela X-1, in which many emission lines are clearly resolved. The evidence of the plasma driven through photoionization is detected. Fluxes of all emission lines, including lines from highly ionized ions, are precisely measured. In addition, the Doppler shifts of the emission lines from H-/He-like ions are measured with an accuracy of  $\sim 100 \text{ km s}^{-1}$  [1]. A spectrum of another HMXB, GX 301-2 is shown in Figure 2. A Compton shoulder is detected in the spectrum of the iron  $K\alpha$  line [2]. In order to reproduce such spectra, models based on simple assumptions (symmetrical geometry, uniform density, uniform ionization structure, single interaction and so on) are not enough.

In this paper, we report about a newly developed Monte Carlo simulator, and introduce examples of its application to observed data. More detailed results of the analyses with the simulator are described in other papers [1, 2]

## 2. Monte Carlo Simulator for High Mass X-ray Binary

In order to understand physical phenomena in photoionized plasmas from precise measured X-ray spectrum, we have developed a Monte Carlo simulator. First, we describe a fully three dimensional geometry, including a matter distribution and an ionization structure. We start the simulation with an X-ray photon. The incident photon interacts with the matter and sometimes generates secondary photons. In the simulation, the incident and all other photons produced by interactions are tracked until they either completely escape the simulation space or are destroyed by some physical processes. The emergent photons are then selected under some conditions which depend on the analysis, and the energy distribution of the selected photons are histogrammed to produce a spectrum. And then, we compare the simulated spectrum with the observed spectrum.

In our simulator, Geant4 [3] is used as the Monte Carlo engine. Geant 4 is a toolkit for the simulation of the passage of particles through matter, and is mainly applied to particle detector simulations. In order to deal with large scale geometries like astrophysical objects and ionized materials in plasmas, we expand the functions of the geometry and the material in Geant4.

A physical process code plays an important role in Monte Carlo simulations. We have developed an original code for physical processes in photoionized plasmas. We account for photoionization, photoexcitation and Compton scattering as for physical processes of X-ray photons. The code is constructed on the premise that photoionization equilibrium is established locally everywhere in the plasma. Therefore, if photoionization take place in the simulation, radiative recombination and radiative transitions to the ground level

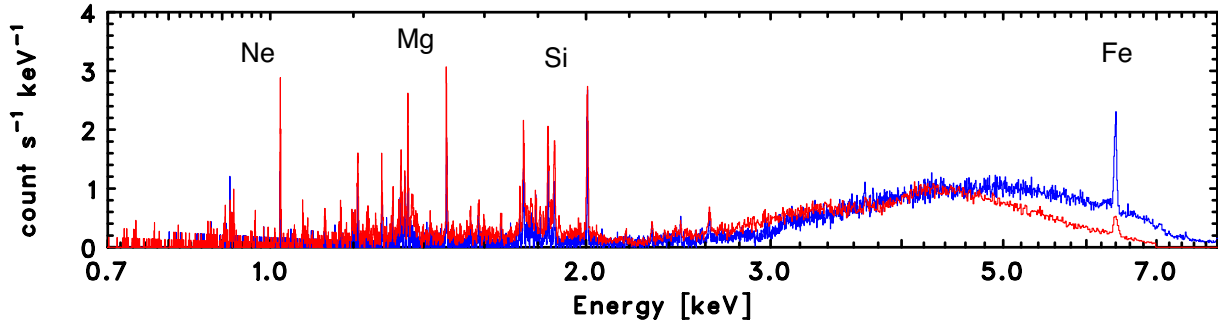


Figure 1: Vela X-1 X-ray spectrum during orbital phase 0.50 obtained with *Chandra* HETGS. The red line shows the spectrum with Medium Energy Grating (MEG), and, the blue one shows the spectrum with High Energy Grating (HEG). Many emission lines result from a photoionized plasma.

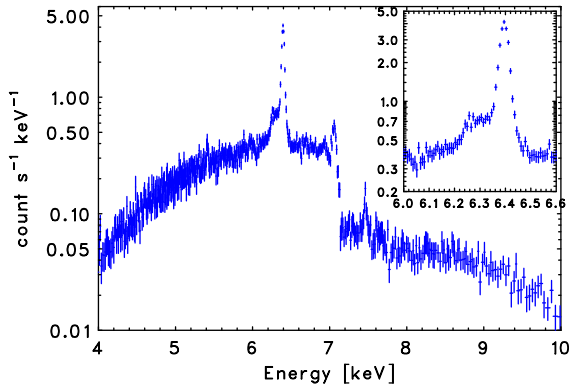


Figure 2: GX 301-2 X-ray spectrum obtained with *Chandra* HETGS. Blow-up of the iron  $K\alpha$  spectrum is also shown. A Compton shoulder is clearly seen in the low energy side of the iron  $K\alpha$  line.

always follow, or fluorescent emissions are induced at the same place, and then, X-ray photons with appropriate energies are generated. In this way, the recombination rate equals with the photoionization rate locally. In the case of photoexcitation, the ion in an excited state produces an X-ray photons by one or more transitions that eventually lead to the ground level. Various emission lines arise as results of such photoionization and photoexcitation.

The cross sections of photoionization and emission line probabilities from recombination cascades are needed for photoionization codes. Transition energies, oscillator strengths, radiative decay rates and line emission probabilities for each excited level to the ground level are required for the photoexcitation codes. We look up a table generated with the Flexible Atomic Code (FAC) [4]. The table is used in our code to handle physical processes.

We took Doppler shifts into account for all of the physical processes. When a photon comes into a region, we calculate cross sections of all physical processes from the photon energy in the co-moving frame. Then, if a physical process is selected and any sec-

ondary photons are generated, energies and directions of the photons are converted to the rest frame.

### 3. Application to the observed data

#### 3.1. Photoionized Stellar Wind in Vela X-1

The emission lines we detected from Vela X-1 are interpreted as due to emission from the stellar wind of the companion star, which is photoionized by the X-ray radiation from the neutron star. In this case, the spectrum emerged from the binary system is the result of the propagation of X-rays through the photoionized stellar wind. Line emission, presumably due to processes, such as photoionization, recombination and fluorescence, are controlled by the ionization structure and the density distribution of the gas in the stellar wind. Therefore, by simulating X-ray propagations in photoionized plasmas, we try to obtain an important clue to addressing the questions about how the photoionized plasma is distributed spatially in the stellar wind and how the distributions can affect the nature of the X-ray emission observed.

First, we calculate an ionization structure of a stellar wind. The ionization structure is determined by the matter distribution of the stellar wind and the spectral shape and the luminosity of the X-ray source. We assume that the velocity structure of the stellar wind is represented by the formulation of the CAK-model [5]. The approximate formula is given as:

$$v(r) = v_{\infty} \left( 1 - \frac{R_{*}}{r} \right)^{\beta}, \quad (1)$$

for a given distance  $r$  from the center of the star, where  $R_{*}$  is the stellar radius and  $v_{\infty}$  is the terminal velocity. We use the  $1100 \text{ km s}^{-1}$  terminal velocity of the stellar wind is given from the results of ultra-violet observations and the fixed  $\beta$  of 0.80 as expected from the assumption by [6]. Given the velocity profile, the

wind density can be calculated by applying the equation of mass continuity, assuming spherical symmetry:

$$n(r) = \frac{\dot{M}_*}{4\pi\mu m_p v(r)r^2}, \quad (2)$$

where  $\dot{M}_*$  is the mass loss rate of the companion star and  $\mu$  is the gas mass per hydrogen atom, and  $\mu = 1.3$  for cosmic chemical abundances. The spectral shape and luminosity of the X-ray source were determined from the X-ray observations. Therefore, once the mass loss rate is provided, the ionization structure of the stellar wind is obtained.

For the obtained ionization structure, a model spectrum can be calculated by the Monte Carlo simulation. And then, we compare the emission lines of the model spectrum with the results obtained from the actual observation. By varying the mass loss rate, we try to find the model which reproduces the observed spectrum.

Figure 3 shows the Vela X-1 spectra obtained from the observations and the model from the Monte Carlo simulation. The mass loss rate of the companion star used in the simulation is  $1.5 \times 10^{-6} M_\odot \text{ yr}^{-1}$ . The upper and the lower panels show the spectra during the eclipse orbital phase and the opposite phase, respectively. The stellar wind with the mass loss rate reproduces the observed X-ray spectra at different orbital phases very well.

By obtaining the model which can explain the observed spectra, we can understand the ionization structure in the Vela X-1 binary system. The ionization structure of the stellar wind is shown in Figure 4. The map shows the sum density of H- and H-like ions of Ne, Mg and Si. In the region between the neutron star and the companion star, both the photoionization rate and the recombination rate are high, and line X-rays from highly ionized ions are produced at high rates.

### 3.2. Compton Shoulder of Iron $K\alpha$ Line in GX 301–2 Spectrum

The Compton shoulder detected in the GX 301–2 spectrum can be used to infer various physical parameters that characterize the scattering medium. In order to obtain some quantitative information from the spectra, we performed Monte Carlo simulations. We assume a spherical cloud with a uniform density and an X-ray continuum source at the center of the cloud. We account for photoionization and subsequent fluorescent emission, as well as Compton scattering by free electrons. The angular dependence of the Compton scattering cross section is fully accounted for and the electrons are assumed to have a Maxwellian energy distribution.

Figure 5 shows some of the results from the simulations for the iron fluorescent line and its Compton

shoulder with varying hydrogen column density ( $N_H$ ) and electron temperature ( $kT_e$ ). The iron  $K\alpha_1$  and  $K\alpha_2$  photons are assumed to be distributed according to the K-shell photoionization rate at each radius from the central continuum source. The power-law photon index is assumed to be  $\Gamma = 1.0$ . In the upper panels of Figure 5, one can see an increase in the scattered flux relative to the narrow line flux as  $N_H$  is increased. The lower panels of Figure 5 show the temperature dependence of the shape of the Compton shoulder. More smearing is seen at higher  $kT_e$ . Photons between 6.24 keV and 6.40 keV are due primarily to single-scattered photons, and the component below 6.24 keV result from multiple-scattering, which are important even at moderate optical depths.

Figure 6 shows two spectra of the iron  $K\alpha$  region (6.0–6.6 keV). One is the spectrum during the first half of the observation, and the other is that during the second half. Each exposure time is 20 ks. Changes in the shape of the Compton shoulder, as well as in the shoulder flux relative to the unscattered line flux, can be seen between the two spectra.

For the two spectra, we performed spectral fits based on the simulation. Models of the spectral fits were generated from the results of the simulations. The parameters of the model are  $N_H$  and  $kT_e$ .

The best-fit models are shown by the lines superimposed on the data in Figure 6. The derived values of  $N_H$  are  $12.0^{+3.5}_{-1.3} \times 10^{23} \text{ cm}^{-2}$  and  $8.5^{+2.3}_{-1.4} \times 10^{23} \text{ cm}^{-2}$  for the first and the second halves, respectively. The difference in the observed Compton profile can be described by a change in the column density, which results in a variation in the number-of-scatterings distribution even at these moderate optical depths. We have also obtained upper-limits (90 % confidence levels) to  $kT_e$  of  $< 3.4 \text{ eV}$  and  $< 0.6 \text{ eV}$  for the first- and second-half spectra, respectively. The detected angular Compton shoulders are evidences that a cold cloud surrounds the X-ray source.

### References

- [1] S. Watanabe et al., “X-ray Spectral Study of Photoionized Stellar Wind in Vela X-1”, in preparation, 2005
- [2] S. Watanabe et al., “Detection of a Fully Resolved Compton Shoulder of the Iron  $K\alpha$  Line in the Chandra X-Ray Spectrum of GX 301–2”, *ApJ*, 597, L37, 2003
- [3] <http://wwwasd.web.cern.ch/wwwasd/geant4/geant4.html>
- [4] <http://kipac-tree.stanford.edu/fac/>
- [5] J.I. Castor, D.C. Abbott, & R.I. Klein, “Radiation-driven winds in Of stars”, *ApJ*, 195, 157, 1975

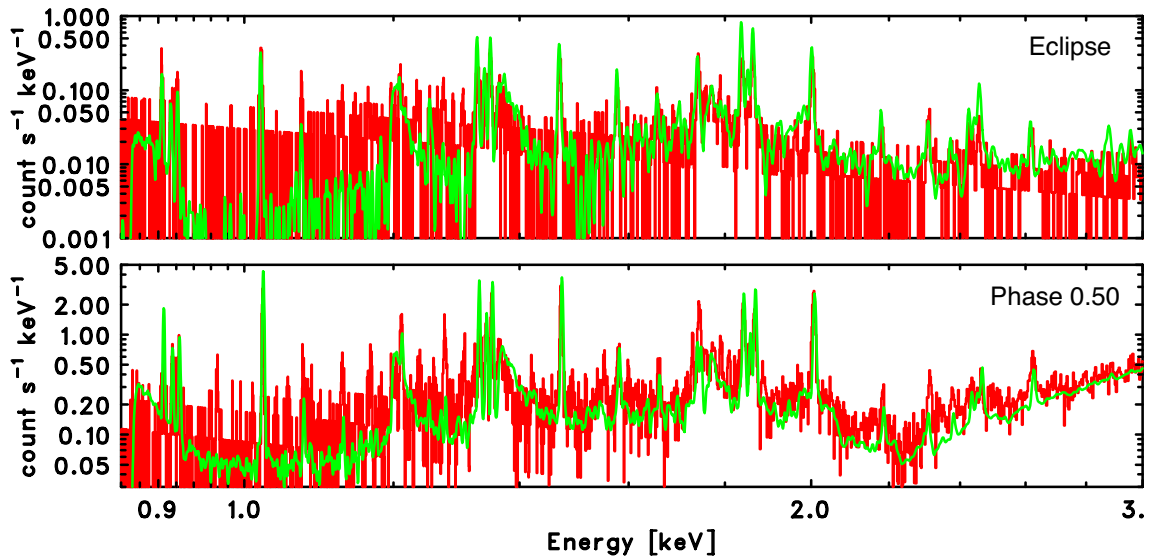


Figure 3: Vela X-1 spectra obtained with Chandra MEG. The upper panel shows the spectrum during the eclipse, and the lower panel shows the spectrum in the phase 0.50. The lines are the model from the Monte Carlo simulation. In the simulation, the stellar wind profile is represented by the CAK-model with the companion star mass loss rate of  $1.5 \times 10^{-6} M_{\odot} \text{ yr}^{-1}$  and the terminal velocity of  $1100 \text{ km s}^{-1}$ .

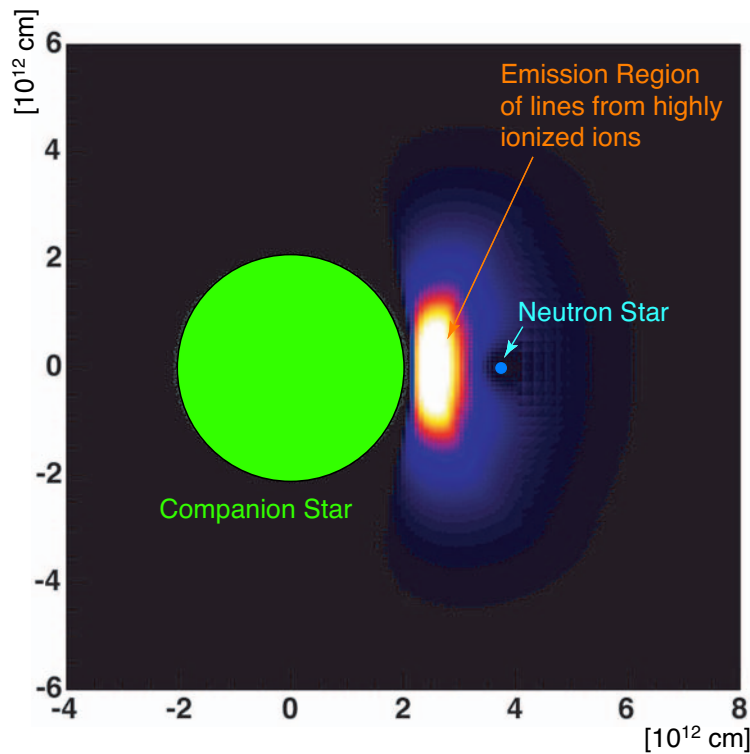


Figure 4: Map of the density of highly ionized ions. The sum of H- and He-like ions of Ne, Mg and Si is shown.

- [6] A. Pauldrach, J. Puls, & R.P. Kudritzki, *A&A*, 164, 86, 1986  
 “Radiation-driven winds of hot luminous stars -  
 Improvements of the theory and first results”,

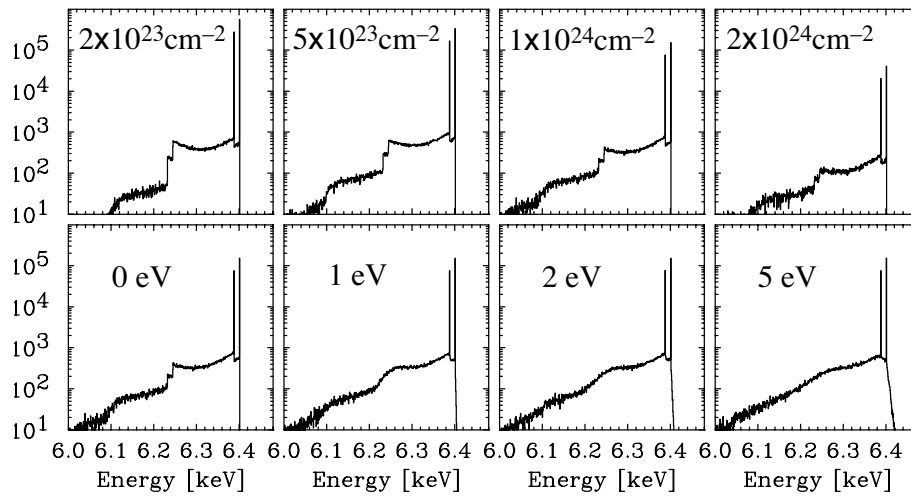


Figure 5: Dependence of the iron  $K\alpha$  line profile on the hydrogen column density ( $N_{\text{H}}$ ) and the electron temperature ( $kT_e$ ). The upper panels show the variation of the iron  $K\alpha$  line and its shoulder as a function of  $N_{\text{H}}$  for a fixed  $kT_e$  at 0 eV. The lower panels show the variation as a function of  $kT_e$  between 0 and 5 eV for a fixed  $N_{\text{H}}$  at  $1 \times 10^{24} \text{ cm}^{-2}$ .

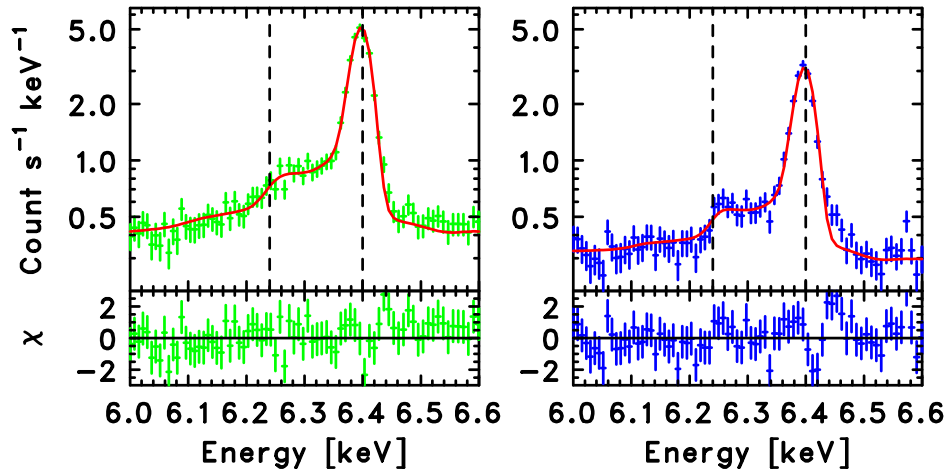


Figure 6: Spectra of the iron  $K\alpha$  region (6.0–6.6 keV). The spectra for the first and the second halves of the observation are shown in the left and the right panels, respectively. Superposed on the data in lines are the best-fit Monte Carlo models.